Miniature Electrodynamic Wireless Power Transmission Receiver Using a Micromachined Silicon Suspension

Miah A. Halim, Adrian A. Rendon-Hernandez, Spencer E. Smith, Joseph M. Samman, Nicolas Garraud, and David P. Arnold, *Senior Member, IEEE*

***Abstract*— We present the design, modeling, fabrication, and experimental characterization of an electrodynamic wireless power transmission (EWPT) receiver for low-frequency (<1 kHz), near-field wireless power transmission. The device utilizes a bulk-micromachined silicon serpentine suspension, two NdFeB magnets and two precision-manufactured coils. The architecture of the transducer is designed to maximize the electrodynamic coupling coefficient while maintaining a low mechanical resonant frequency in order to maximize the power density for low-frequency wireless power transmission. An equivalent lumped-element circuit model is established to parameterize the system and to predict the output performance of the proposed system. A prototype device is fabricated, assembled and tested, and the results are compared with the model prediction. The 0.31 cm^3 device generates 2.46 mW average power (7.9 mW · cm^{-3} power density) at 4 cm distance from a transmitter coil operating at 821 Hz and safely within allowable human exposure limits. This data corresponds to a normalized power density of 21.9 mW · cm^{-3} · mT^{-2}, which is 44% higher than similar reported devices. Based on these results, this device shows great suitability for wirelessly charging mobile, wearable and bio-implantable devices. [2020-0161]**

***Index Terms*— Wireless power transmission, electrodynamic coupling, bulk-micromachining, serpentine suspension, torsional resonance, electromechanical transducer.**

I. Introduction

With great progress of microelectronic industries over the past several decades, electronic devices such as mobile phones, tablets, wearable devices, laptop computers, etc. have become essential elements in our daily life. The proliferation of these devices creates the need for incessant re-charging and a bewildering number and variety of charging cables. Plugging in a cable to recharge a phone or tablet is a necessary inconvenience. However, charging of smaller wearable devices (e.g. smart watches, fitness trackers, assistive hearing devices) poses additional burdens, both technical and practical. First, these devices have smaller and more complicated form factors (curved surfaces, limited locations for charging port, need for water-proofing). Second, in almost all cases, the user must doff the device for re-charging. Modern implantable medical devices pose even additional challenges. Most use primary (single-use) batteries, and require recurrent battery replacement surgeries. For all these applications, wireless recharging would be an ideal solution, and therefore, significant attention has been focused on the development of wireless power transmission (WPT) systems [1]–[3].

The most common WPT systems transmit power via electromagnetic or acoustic fields and can be categorized into either near-field (non-radiative) and far-field (radiative) approaches [4]. Most research and commercial product development has focused on the near-field electromagnetic WPT approaches, which can be further subdivided into three primary categories based on the coupling between the transmitter and receiver: inductive, magnetic resonance (a special case of inductive) and capacitive. These approaches offer efficient power transmission over distances ranging from several millimeters to several centimeters, and make use of electromagnetic fields ranging from 100 kHz to 10 MHz [5]–[7].

As new methodologies enable larger wireless transmission distances, there are important technical and safety considerations regarding the electromagnetic fields that exist in between the transmitter and receiver. First, there are strict limits to the amplitude of the magnetic fields that can be applied to humans [8], [9]. Second, in the case where there may be any electrically conductive media, the relatively high-frequency inductive/capacitive coupled systems tend to generate eddy (Foucault) currents [10]. These eddy currents can attenuate or alter the fields used for power transmission and may also cause undesirable or even unsafe heating in the intervening objects. Similarly, the use of any materials with high electrical permittivity or high magnetic permeability must be carefully analyzed.

As a possible solution in addressing these constraints, particularly for wearables and medical implants, the use of magnetic near-fields at much lower frequencies (<1 kHz) have

Manuscript received May 13, 2020; revised August 28, 2020; accepted December 12, 2020. Date of publication January 1, 2021; date of current version January 15, 2021. This work was supported in part by the National Science Foundation (NSF) Industry/University Cooperative Research Centers (I/UCRC) on Multi-Functional Integrated System Technology (MIST) Center under Grant IIP-1439644, Grant IIP-1439680, and Grant IIP-1738752. Subject Editor S. M. Spearing. *(Corresponding author: Miah A. Halim.)*

Miah A. Halim, Adrian A. Rendon-Hernandez, Spencer E. Smith, Joseph M. Samman, and David P. Arnold are with the Interdisciplinary Microsystems Group (IMG), University of Florida, Gainesville, FL 32611 USA (e-mail: md.miah@ufl.edu; arendonhernandez@ufl.edu; smithspencer12@ufl.edu; jsamman@ufl.edu; darnold@ufl.edu).

Nicolas Garraud was with the Interdisciplinary Microsystems Group (IMG), University of Florida, Gainesville, FL 32611 USA. He is now with Alternative Energies and Atomic Energy Commission (CEA-LETI), 38054 Grenoble, France (e-mail: nicolas.garraud@cea.fr).

Color versions of one or more figures in this article are available at https://doi.org/10.1109/JMEMS.2020.3045350.

Digital Object Identifier 10.1109/JMEMS.2020.3045350

been considered in order to mechanically resonate a permanent magnet in the receiver [11], [12]. The use of lower frequencies facilitates higher field safety margins, significantly better penetration through conductive media (e.g., metal, human body, fabrics etc.) and nearly eliminates the generation of eddy currents and its possible effects (e.g., parasitic heating) [4]. Furthermore, by leveraging mechanical resonance in the receiver, longer range and higher power density transduction can be achieved, as compared to simple induction [13].

Electrodynamic transduction refers to the bi-directional electromechanical interaction/coupling between a permanent magnet and coil. In an electrodynamic WPT (EWPT) system, a time-varying magnetic field is generated by ac current in a transmitter coil, which is used to excite the physical motion of a magnet in the receiver. The mechanical motion of the magnet in the receiver is converted into electricity by one or more electromechanical transduction schemes contained within the receiver (e.g. electrodynamic/induction, piezoelectric, or capacitive). Furthermore, the mechanical motion of the magnet can be continuous (i.e. spinning) or oscillatory, and the oscillatory motion might be rectilinear, torsional, or a combination thereof [12]–[17]. EWPT concepts using torsional oscillation of the receiver magnet have been shown to be particularly effective in terms of both efficiency and maximum power transmission [12]. Experiments on through-body and multi-receiver transmissions have also been demonstrated [16], [17].

As an alternative to use of electrodynamic transduction in the receiver, piezoelectric transducers have also been introduced in [18], [19]. A more sophisticated center-clamped piezoelectric cantilever with magnetic tip masses has also been investigated where a theoretical lumped element model was derived and experimentally verified [20]. Differing from simple cantilevered structures, an EWPT receiver using a torsionally resonant meandering beam structure with multiple piezoelectric transducers was experimentally demonstrated in [21]. While great strides have been made to demonstrate and evaluate various approaches, all of the EWPT systems described above utilized relatively bulky, hand-assembled receivers to demonstrate their functionalities. For potential use in wearable or implantable applications, a much smaller, and higher-performance design solution is needed.

Our group has recently reported a chip-scale microfabricated EWPT receiver by utilizing micromachined silicon (Si) serpentine suspension, off-the-shelf magnets and hand-wound coils [22]. However, the receiver suffered from poor electrodynamic coupling between the receiver magnet and receiver coil and a very low voltage sensitivity, which made downstream ac/dc rectification and power management electronics very challenging. A more recent improved version of the device uses a more volume-efficient design, high-Q torsional resonance, and precision micro-manufacturing/ micro-assembly that together offers 19× stronger electrodynamic coupling, 16× better magnetic field sensitivity, as well as 1.7× higher power density [23]. In this paper, we extend this previous conference publication [23], which reported only the fabrication and experimental characterization, by a) elaborating on the design and modeling of the serpentine suspension and transducer elements, b) presenting a lumped element equivalent electrical circuit model to analyze and predict the system performances, and c) comparing the model with experimental results.

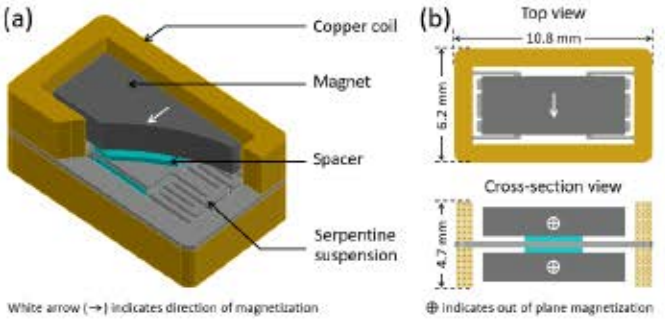

Fig. 1. (a) Schematic structure of the proposed electrodynamic wireless power transmission (EWPT) receiver using serpentine suspension and (b) its top and cross-section views.

II. EWPT Micro-Receiver Design and Modeling

A. Receiver Structure and Its Operation

Figure 1 shows the schematic structure of the proposed EWPT receiver with a torsionally resonated center platform supported by a serpentine beams suspension to a surrounding frame. The design uses two magnets, attached to both sides of the center platform, to oscillate under the influence of an external time-varying magnetic field. Two rectangular-shaped coils are attached to both sides of the base frame with the coils electrically connected in series. The magnet-coil-suspension structure forms a resonant electrodynamic transducer for power generation. To maximize performance, each magnet occupies the entire area over the serpentine suspension beams and is magnetized along its lateral direction (perpendicular to the rotation axis). A spacer is used between each magnet and the center platform to allow clearance between the magnet and the suspension beam-sections during torsional oscillation. As compared to the previous proof-of-concept design [22], the advantages of using larger magnets include: more effective use of the volume within the device that reduces the dead space; increased sensitivity to the external magnetic fields; and more magnetic flux linkage with the coils that results in stronger electrodynamic coupling. Because the two magnets are mechanically fixed to the suspension, from here onward, we will refer to only the 'magnet'. Similarly, the two series connected coils will be referred to as the 'coil'.

Figure 2 illustrates the electrodynamic operation principle of the proposed EWPT receiver structure. An alternating current I_S supplied to a transmitter coil generates spatially distributed, time-varying magnetic field of desired frequency and amplitude. This field induces a torsional oscillation of the magnet in the micro-receiver, wherein the motion of the magnet induces voltage (technically an electromotive force, or emf) in the receiver coil via Faraday's law. Electrical current I_L (and hence power) is delivered to an external load connected to the receiver coil. Maximum voltage and power generation are achieved at torsional resonance of the mechanical suspension

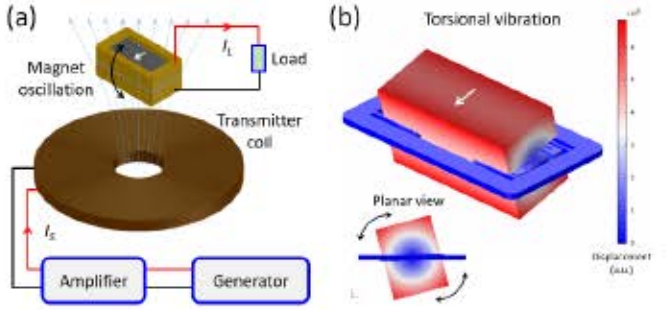

Fig. 2. (a) Principle of electrodynamic wireless power transmission (EWPT) with the proposed receiver structure and (b) torsional vibration of the receiver magnets in response to the time-varying magnetic fields supplied by the transmitter coil.

and also when the receiver magnet is oriented perpendicular to the magnetic field. Note that, the direct inductive coupling between the transmitter coil and the receiver coil is negligible (very low mutual inductance) since the system is designed to operate at low frequencies (<1 kHz) [12].

B. Design Procedures

While designing and optimizing the mechanical suspension structure, special care needs be taken to achieve large electrodynamic coupling. The following prerequisites have been chosen and used as design inputs: size of the magnets, resonant frequency, maximum rotation amplitude of the magnets, and suspension thickness and its material properties (Young's modulus, Poisson's ratio and density). Several other constraints and design objectives to be considered including compact design with minimal suspension length and reduced volume; compliant mechanical suspensions of the desired vibration mode (here torsional rotation), while avoiding other spurious modes around the resonant frequency of interest; stress on the mechanical suspension at the maximum rotation amplitude to be lower than its yield stress.

In the design process, we considered four different torsional suspension architectures of a fixed base frame, and a mounting platform, within the same footprint ($10.8 \times 6.2 \times 0.3$ mm^3). Figure 3 shows the schematics of the suspensions with corresponding beam types: simple torsion beams (design A), split-anchor beams (design B), serpentine beams (design C), and split-anchor serpentine beams (design D). In all four designs, the beam sections parallel and perpendicular to the axis of rotation have the same width and the same gap between them is maintained.

The resonance behavior of four designs are modeled by 3D finite element analysis (FEA) simulation using COMSOL Multiphysics. The compliant epoxy adhesive layer—bonding the magnets and spacers to the meandering suspension—is simulated via a 20-μm-thick elastic layer condition with the following properties: Young's modulus $E = 2$ GPa and Poisson's ratio $\nu = 0.25$. FEA modal analyses indicate that the 1st and 2nd vibration modes for all four designs correspond to torsional rotation about x-axis and translational displacement along z-axis, respectively. However, the 3rd mode corresponds to torsional rotation about y-axis for the designs A and B, and

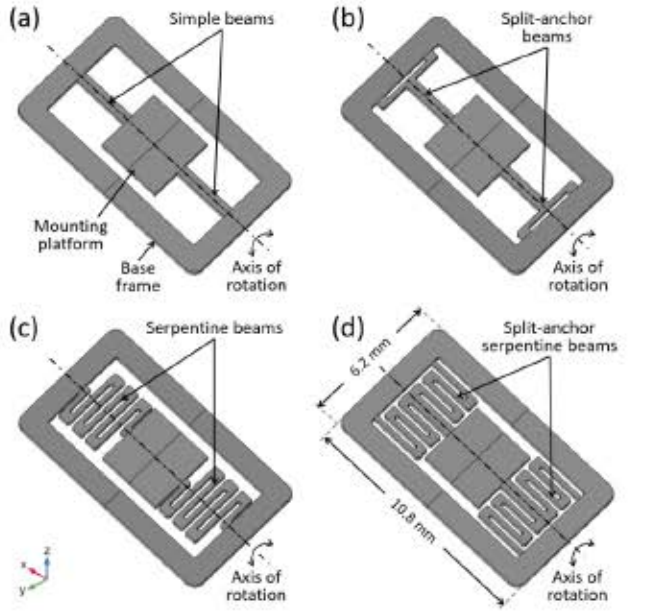

Fig. 3. Schematics of the mechanical suspensions considered for the EWPT receiver design within the same footprint: (a) design A- simple torsion beams, (b) design B- split-anchor beams, (c) design C- serpentine beams, and (d) design D- split-anchor serpentine beams.

translational displacement along the y-axis for the designs C and D. Figure 4 shows, as an example, the mode shapes of the EWPT receiver using design D (split-anchor serpentine beams suspension). Figure 5 shows the frequency response for the torsional rotation about the x-axis of the receiver with design D using a damping ratio $\zeta = 0.003$, corresponding to a Q-factor of 165 (as measured experimentally). In the plot, no peaks are observed for translational displacement modes (at 1073 Hz and at 1300 Hz) since there is no torsional response for those modes.

In order to investigate the mechanical reliability of each design, FEA simulations are performed for various magnetic field amplitude excitations at torsional (1st mode) resonance. Two mechanical limits are considered: 1) the maximum rotation angle at which the magnets make contact with the coil ($\pm 21.5°$ for designs A, B and C) or suspension beams ($\pm 11.3°$ for design D) and 2) the maximum rotation angle before the beams may fail due to stress. Considering the brittleness of silicon, it is assumed a catastrophic failure would occur whenever the largest principal normal stress exceeds the ultimate tensile strength of silicon (assumed to be $\sigma_{UT} = 165$MPa). Special attention is paid to the distribution of the first and third principal stresses (σ_1 and σ_3) on the suspension base at the maximum torsional rotation. Figure 6(a) shows a plot of maximum first principal stress vs. rotation angle for all four designs. It is evident from the figure that the stress-related failure will occur before the receiver magnets for designs A, B and C reach their maximum rotational limit. For design D, the magnets will interfere with the beam-sections before exceeding the stress-related failure limit. As shown in figure 6(b), the simulations for design D predict that at the maximum rotation angle of $\pm 11.3°$, the maximum stress

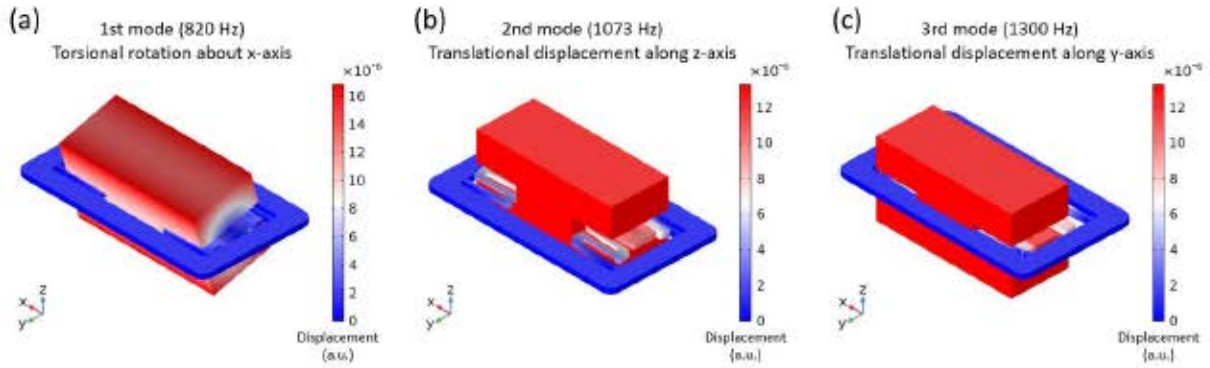

Fig. 4. Modal analysis of the EWPT receiver using split-anchor serpentine beams suspension (design D) to illustrate its mechanical resonance: (a) torsional mode, (b) bending mode, and (c) lateral displacement mode.

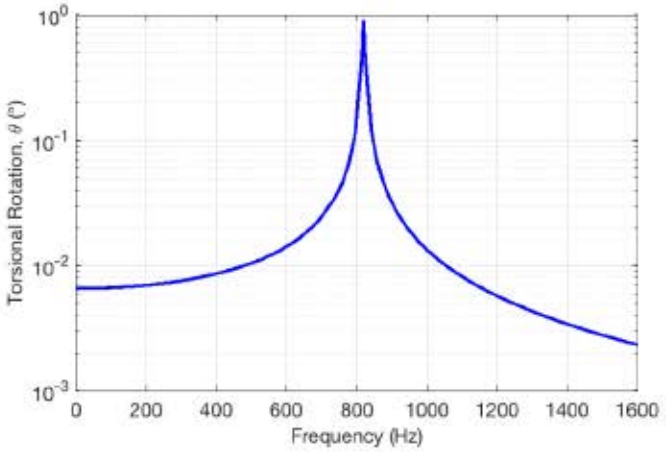

Fig. 5. FEA simulated frequency response for the torsional rotation about the x-axis of the receiver magnet of design D for an applied field of 50 μT_{rms}, and a damping ratio $\zeta = 0.003$ (Q = 165).

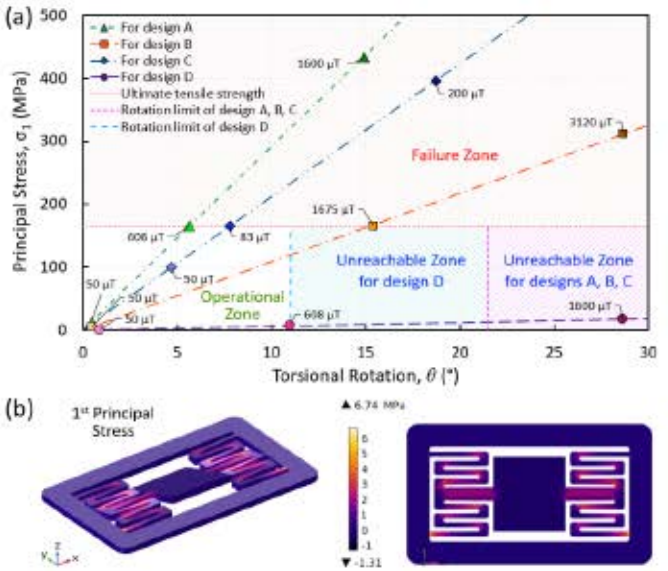

Fig. 6. FEA simulation results of the reliability study: (a) failure diagram for the maximum stress and permissible torsional rotation showing the operational, unreachable and failure zones, (b) principal stress distribution on the suspension base of design D when an external field of 608 μT_{rms} is applied in dynamic loading at 820 Hz resonance (magnet and spacer not shown).

is only about 6.7 MPa for which the required B-field is 608 μT_{rms}.

Table I summarizes the FEA simulation results obtained from each suspension design. Among these designs, design D (split-anchor serpentine beams suspension) has been selected based on the following aspects: (i) designs C and D satisfy the requirement of low-frequency operation (<1 kHz) for the intended mode of oscillation i.e., the torsional mode, (ii) from these two designs, design D shows about one order of magnitude higher torsional stiffness when compared to design C which offers a better mechanical reliability, (iii) design D also offers higher off-axis stiffnesses than design C that does not come in the way during the receiver's torsion mode operation. (iv) finally and most importantly, design D offers the largest rotation (±11.3°) of the magnets while keeping the stresses well below the stress-related failure limit (see figure 6a).

Once the mechanical suspension is successfully designed, the other element in the design procedure to be considered is the transducer: an electrodynamic transducer, in this case. Since the magnetic moment $\vec{m}$ of a permanent magnet depends on its volume v_{mag} [12], a larger permanent magnet is desirable (and therefore, has been used) that facilitates the flux linkage with the receiver coil, under a given magnetic field generated by the transmitter. Additionally, a perfectly wound receiver coil placed as close as possible to the magnet (magnet-coil airgap should not prevent the magnet's torsional rotation) strengthens the electrodynamic coupling and the overall device performance. Here, a 0.5 mm magnet-coil air gap is maintained that leaves adequate clearance for ±11.3° rotation of the magnet. To first order, the wire gauge does not significantly affect the generated power; however, a small wire diameter (more turns for a given volume) is generally preferred to obtain larger voltages (lower currents) to ease the system-level voltage rectification and power management challenges. Here, a fine 44 AWG (American wire gauge) magnet wire is chosen for ease of handling/manufacturing. The wire is wound into 498-turn rectangular coils that fill the $8.8 \times 4.2 \times 2.2$ mm^3 volume around the magnet but maintain the 0.5 mm magnet-coil clearance (refer to figure 1).

TABLE I
SUMMARY OF THE FEA SIMULATION RESULTS OBTAINED FROM THE SUSPENSION DESIGN

Mode	Parameter	Design A	Design B	Design C	Design D
1st	Type of mode	Torsional rotation [a]	Torsional rotation [a]	Torsional rotation [a]	Torsional rotation [a]
	Resonant frequency	1244 Hz	1259 Hz	346 Hz	820 Hz
	Torsional stiffness	9.33×10^{-2} N.m.rad^{-1}	9.55×10^{-2} N.m.rad^{-1}	7.25×10^{-3} N.m.rad^{-1}	4.28×10^{-2} N.m.rad^{-1}
	Rotation angle limit	± 21.5 °	± 21.5 °	± 21.5 °	± 11.3 °
	Rotation angle at stress-related failure	± 5.6 °	± 15.3 °	± 7.9 °	Unreachable
	Required B-field for stress-related failure	608 μT_{rms}	1675 μT_{rms}	83 μT_{rms}	Unreachable
	Required B-field at rotation-related failure	N/A	N/A	N/A	608 μT_{rms}
2nd	Type of mode	Displacement [b]	Displacement [b]	Displacement [b]	Displacement [b]
	Resonant frequency	2224 Hz	1584 Hz	441 Hz	1073 Hz
	Flexural stiffness	1.17×10^{5} N.m^{-1}	5.96×10^{4} N.m^{-1}	4.51×10^{3} N.m^{-1}	2.74×10^{4} N.m^{-1}
3rd	Type of mode	Torsional rotation [c]	Torsional rotation [c]	Displacement [d]	Displacement [d]
	Resonant frequency	2628 Hz	2206 Hz	509 Hz	1300 Hz
	Torsional/Translational stiffness	1.08 N.m.rad^{-1}	0.76 N.m.rad^{-1}	7.27×10^{3} N.m^{-1}	4.03×10^{4} N.m^{-1}

[a] about x-axis, [b] along z-axis, [c] about y-axis, [d] along y-axis, N/A indicates the design is already in the failure zone before reaching its rotational limit.

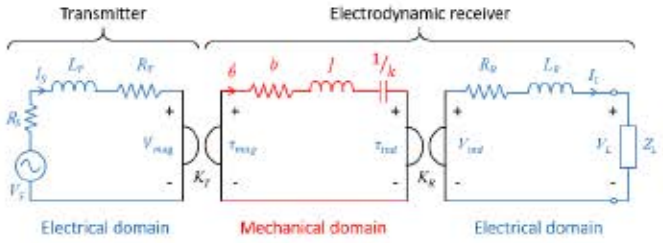

Fig. 7. Equivalent electrical circuit of the EWPT system showing the energy flow between electrical and mechanical domains via electrodynamic coupling.

C. Equivalent Circuit Model

The multi-energy-domain system is modeled using a lumped element modeling approach [24]. This approach facilitates physics-based understanding of the system dependencies as well as modeling the behavior of the system using ordinary differential equations (specifically here the time-harmonic steady-state behavior represented as an equivalent circuit and solved using ac circuit analysis). The schematic electrical circuit of the EWPT system is shown in figure 7. The three sections of the equivalent model respectively represent the electrical behavior of the transmitter, the mechanical behavior of the resonating magnet (here specifically the rotational mechanics), and the electrical behavior of the receiver. The primary system variables include phasor voltages, currents, torques, and angular velocities. All phasor amplitudes will be reported as root-mean-square (rms), unless otherwise noted.

Electromechanical coupling (linkages) between the electrical and mechanical domains are achieved through electrodynamic coupling represented by a gyrator circuit element. For an ideal (neither stores nor dissipate energy) two-port gyrator [25], the relationships for the two couplings are given by

$$K_T = \frac{\tau_{mag}}{I_S} = \frac{V_{mag}}{\dot{\theta}} \tag{1}$$

$$K_R = \frac{\tau_{ind}}{I_L} = \frac{V_{ind}}{\dot{\theta}} \tag{2}$$

where K_T and K_R are, respectively, the transmitter and receiver electrodynamic transduction coefficients (units of $\mathrm{N \cdot m \cdot A^{-1}}$ or $\mathrm{V \cdot s \cdot rad^{-1}}$). The magnetic fields produced by the coil are not explicitly expressed in the equivalent circuit model, but will be discussed further below. Ultimately it is the physical arrangement of the magnet and coils that determine the coefficients K_T and K_R.

In the first electrical domain, a power source with source resistance R_S supplies an ac voltage V_S and ac current I_S to a transmitter coil, represented by an electrical resistance R_T and inductance L_T. In the mechanical domain, the mechanical oscillator is represented by torsional spring stiffness k, mass moment of inertia J and torsional damping coefficient b. The oscillator is subjected to two electrodynamic torques: a torque $\vec{\tau}_{mag}$ from currents in the transmitter coil and a torque $\vec{\tau}_{ind}$ from currents in the receiver coil. Similarly, the rotational motion of the magnet $\dot{\theta}$ induces voltages V_{mag} and V_{ind} in the transmitter and receiver coils, respectively. Finally, in the second electrical domain, the receiver coil, represented by a resistance R_R and inductance L_R, is connected to an arbitrary load impedance Z_L. In principle, each of the lumped element parameters can be predicted as *a priori* via relevant dimensions and material properties. Alternatively, most of the system parameters can also be determined via appropriate experimental tests. In this work, a combination of approaches will be used, since some parameters may be easier to calculate, whereas some parameters may be easier to measure/infer.

D. Magnetic Fields, Torques, and Electrodynamic Couplings

The transmitter coil used in this work is a multi-layer, multi-turn pancake type coil of inner diameter d_1, outer diameter d_2 and thickness l, having N turns. The field produced by the transmitter coil is modeled by a short-solenoid formula, where the amplitude of the on-axis magnetic field along the z-axis (refer to figure 2) is calculated as [12]

$$B_z = \frac{\mu_0 N I_S}{2l(d_2 - d_1)} \left[(l + 2z) \ln\left(\frac{a_1}{a_2}\right) + (l - 2z) \ln\left(\frac{a_3}{a_4}\right) \right] \tag{3}$$

where $a_1 = d_2 + \sqrt{d_2^2 + (l + 2z)^2}$, $a_2 = d_1 + \sqrt{d_1^2 + (l + 2z)^2}$, $a_3 = d_2 + \sqrt{d_2^2 + (l - 2z)^2}$, $a_4 = d_1 + \sqrt{d_1^2 + (l - 2z)^2}$ and z is the distance from the centroid of the transmitter coil.

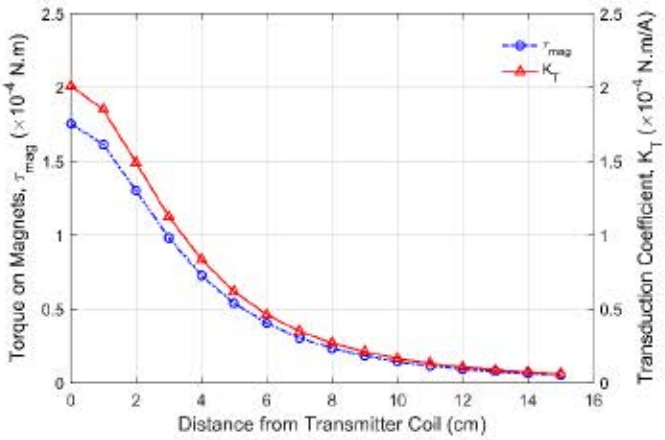

Fig. 8. Simulated torque on the receiver magnet and the transmitter transduction coefficient at various distances from the transmitter coil with 2 mT_{rms} field generated at the centroid of the coil.

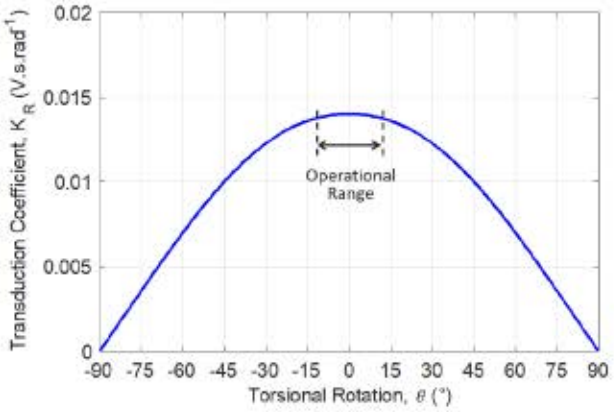

Fig. 9. Simulated receiver transduction coefficient as a function of the torsional rotation of the receiver magnet.

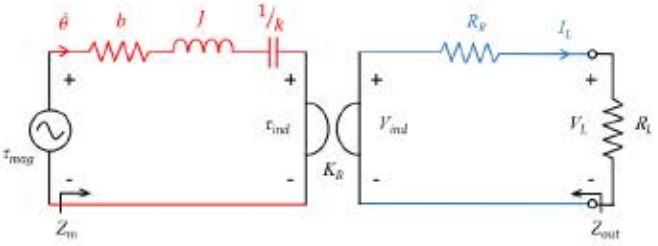

Fig. 10. Simplified equivalent electrical circuit of the EWPT receiver.

For modeling and experimental purposes, the magnetization axis of the receiver magnet is oriented perpendicular to the magnetic field generated by the transmitter coil, so as to maximize the torque acting on the magnet. In this configuration, the torque induced on the receiver magnet is

$$\tau_{mag} = \left|\vec{m} \times \vec{B}_z\right| = \frac{B_r}{\mu_0} v_{mag} B_z \tag{4}$$

where $\vec{m} = \vec{M} v_{mag}$ is the net magnetic moment of the receiver magnet in which v_{mag} is the magnet volume and $\vec{M}$ is the magnetization of the magnet. Assuming ideal magnetization, $\left|\vec{M}\right| = B_r/\mu_0$ where B_r is the remanence and μ_0 is the free space permeability. Note that the magnetic field gradients produced by the transmitter coil could also produce forces acting on the magnet, but since the rotation angles are assumed small, the forces are assumed to be negligible.

In the experiments, both the ac current to the transmitter coil I_S and the magnetic field B_z are carefully measured and controlled. Substituting (3) into (4), one can derive an explicit expression for the excitation torque,

$$\tau_{mag} = \frac{N B_r v_{mag} I_S}{2l(d_2 - d_1)} \left[(l + 2z) \ln\left(\frac{a_1}{a_2}\right) + (l - 2z) \ln\left(\frac{a_3}{a_4}\right) \right] \tag{5}$$

and using (1), so too the transmitter electrodynamic coupling coefficient K_T.

$$K_T = \frac{N B_r v_{mag}}{2l(d_2 - d_1)} \left[(l + 2z) \ln\left(\frac{a_1}{a_2}\right) + (l - 2z) \ln\left(\frac{a_3}{a_4}\right) \right] \tag{6}$$

To stay within allowable human exposure limits [8], [9], the magnetic field is limited such that a maximum 2 mT_{rms} field is produced at the centroid of the coil. According to the IEEE standard [9], a maximum permissible magnetic field (in controlled environment) for exposure of the head and torso at 820 Hz is 2.51 mT_{rms}. Figure 8 shows how the torque $\vec{\tau}_{mag}$ and transmitter electrodynamic transduction coefficient K_T change with the distance between the transmitter and the receiver. Both torque and K_T follow the same decreasing trend as the field decreases with the increase in the distance.

In order to model the receiver electrodynamic coupling coefficient K_R, the flux interaction between the receiver magnet and receiver coil are computed using a MATLAB script that relies on the calculated magnetic field produced by a cuboidal magnet [27]. Note that for the sake of simplicity, a single magnetic volume having equivalent height to the two-magnets final arrangement surrounded by coils is considered. The value of the transduction coefficient depends on the rotational angle of the magnet, as shown in figure 9. Within the operational range (±11.3°), K_R is nearly constant. For later computation purposes, the peak value of $K_R = 0.014$ V · s · rad^{-1} is used.

E. System Analysis

For later comparison with experimental results, as shown in figure 10, a simplified model of the EWPT micro-receiver is considered with the following simplifications. First, the torque generated by the transmitted field source τ_{mag} is well controlled during the experiments, so an ideal torque source is used in the model (eliminating the need to model the transmitter coil). Second, at low frequencies (<1 kHz), the coil reactance is much smaller than its resistance ($\omega L_R \ll R_R$) and so L_R is neglected; specifically in the device $R_R = 250\Omega$ and $\omega L_R = 25\Omega$ at 821 Hz. Third, the complex load impedance Z_L is replaced with a resistive load R_L, since the output impedance at resonance will be purely real and hence the optimal load will also be real.

Using standard circuit analysis, it can be shown (see Appendix) that the frequency-dependent load voltage for

an arbitrary load resistance is

$$V_L = \frac{\tau_{mag} K_R}{\left(b + j\omega J + \frac{k}{j\omega}\right)(R_R + R_L) + K_R^2} R_L \tag{7}$$

In order to explicitly describe the system performance, three special cases are discussed below.

Case I (Open-Circuit): When there is no external load connected, the frequency-dependent open circuit voltage output is

$$V_L|_{R_L=\infty} = \frac{\tau_{mag} K_R}{\left(b + j\omega J + \frac{k}{j\omega}\right)} \tag{8}$$

Case II (Resonance): At resonance i.e., when $\omega = \omega_r = \sqrt{k/J} = 2\pi f_r$, where f_r is the resonant frequency in Hz, the impedance due to torsional spring stiffness k and the mass moment of inertia J cancel which, (for a given load resistance) maximizes the rotational displacement, angular velocity, and load voltage and time-averaged load power. In this case,

$$V_L|_{\omega=\omega_r} = \frac{\tau_{mag} K_R}{b(R_R + R_L) + K_R^2} R_L \tag{9}$$

$$P_L|_{\omega=\omega_r} = \frac{V_L^2}{R_L} \tag{10}$$

where (10) assumes V_L is the rms voltage (as opposed to peak voltage).

Case III (Resonance + Optimal Load): For maximum power transfer to a load, the optimal load is the complex conjugate of the output impedance of the system $Z_{L\_opt} = Z_{out}^*$. At resonance ($\omega = \omega_r$), the total output electrical impedance is purely real, and consequently the optimal load resistance is

$$R_{L\_opt} = \frac{K_R^2}{b} + R_R = R_R(\gamma + 1) \tag{11}$$

Here, $\gamma = K_R^2/bR_R$ is a unitless parameter called 'electrodynamic coupling strength' that represents the electromechanical energy conversion effectiveness of an electrodynamic transducer [26]. Therefore, the corresponding load voltage and maximum time-average load power become

$$V_{opt} = V_L|_{\substack{\omega=\omega_r \\ R_L=R_{L\_opt}}} = \frac{\tau_{mag} K_R}{2b} \tag{12}$$

$$P_{max} = P_L|_{\substack{\omega=\omega_r \\ R_L=R_{L\_opt}}} = \frac{\tau_{mag}^2 K_R^2}{4b^2 R_{L\_opt}} \tag{13}$$

It is evident from (12) and (13) that the output performance (voltage and power) of the EWPT receiver greatly depends on the torque τ_{mag} on the receiver magnet. The higher the torque is, the higher the electrodynamic couplings (K_T, K_R) will be. Eqn. (4) indicates that the amount of torque on a magnet depends on the volume of the magnet v_{mag}; torque increases with the increase in the magnet volume. Therefore, a larger magnet is better, but effectively makes the overall size of the EWPT receiver bigger. Moreover, the size of the EWPT receiver is constrained by the specific end-use application. To first-order approximation, the power scales with the volume, and hence maximizing the power density (power per volume) of this type of electrodynamic receiver is a key design objective.

TABLE II
FIXED SYSTEM PARAMETERS USED FOR ANALYTICAL SIMULATION

Parameter	Value
Inner diameter of transmitter coil, d_1	5 cm
Outer diameter of transmitter coil, d_2	15 cm
Thickness of the transmitter coil, l	1.5 cm
Resistance of the transmitter coil, R_T	305 mΩ
Inductance of the transmitter coil, L_T	2.6 mH
No. of turns in the transmitter coil, N	169
*Resistance of receiver coil, R_R	250 Ω
*Inductance of receiver coil, L_R	4.8 mH
*No. of turns of receiver coil	996
Volume of the receiver magnet	8×10^{-8} m^3
Torsional mass moment of inertia, J	1.61×10^{-9} Kg.m^2
Torsional spring stiffness, k	4.28×10^{-2} N.m.rad^{-1}
Torsional damping coefficient, b	5.03×10^{-6} N.m.s.rad^{-1}
Residual flux density of the magnet, B_r	1.38 T
Receiver electrodynamic coupling, K_R	0.011 V.s.rad^{-1}
Permeability of free space, μ_0	$4\pi \times 10^{-7}$ N.A^{-2}

*Combined values for the two series-connected receiver coils

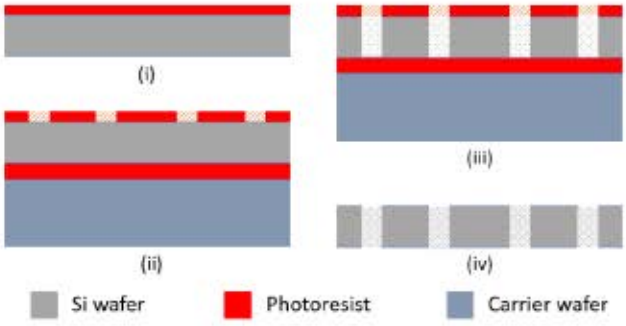

Fig. 11. Schematics of the Si serpentine suspension micro-fabrication process flow for the EWPT receiver.

The simulation parameters used in the analytical calculation are shown in Table II, which have been derived from the geometry and material properties of the device components. Note that the value of K_R is calculated using (11), from experimentally determined γ and b. This measured K_R value (in Table II) closely matches with the simulated value discussed earlier (in Figure 9).

III. PROTYPE FABRICATION AND ASSEMBLY

A. Micro-Fabrication of the Mechanical Suspension

The base frame / split-anchor serpentine beams structure (and the spacers) are fabricated by through-etching a 300 μm thick double-side-polished, 4-inch Si wafer, as illustrated in figure 11. A single mask photolithography process is used. First, the wafer is coated with 11 μm thick photoresist (AZ9260) and is baked on a hotplate at 112°C for 3 min, after regular wafer cleaning and HMDS treatment. The photoresist is then exposed using the specific mask with appropriate exposure dose and is developed using 3:1 DI water:AZ400K developer for 6 min. Then, the patterned wafer is bonded to a carrier wafer (500 μm thick, single-side-polished, 4-inch Si wafer) by using the same thick photoresist. The wafer stack is baked for an additional ~15 min to drive off the solvent from the resist in the bond layer. The resist residue in normally cleared areas of the pattern of the bonded sample is

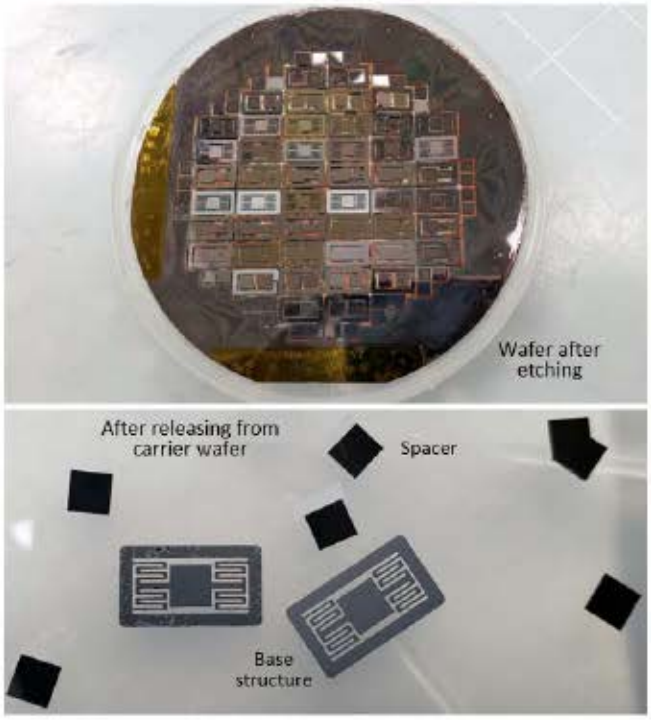

Fig. 12. Photographs of the micro-fabricated Si serpentine suspension structures and the spacers for the EWPT receiver.

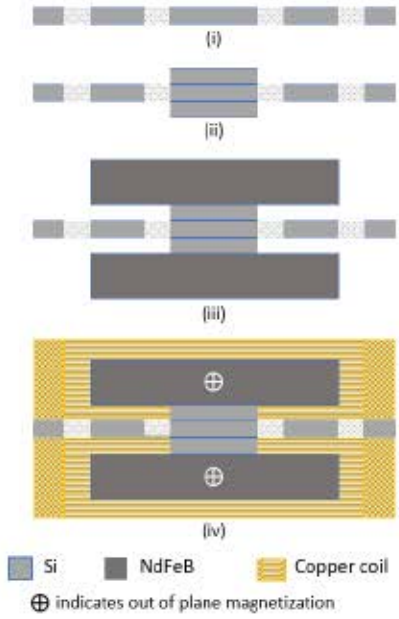

Fig. 13. Schematics of the EWPT receiver assembly process steps.

then removed by oxygen plasma ashing at 300 W, 300 sccm for 1 min. Then, through-etching of the patterned sample is done by deep reactive-ion etching (DRIE). Once done, each individual structure is released on the carrier wafer which is then cleaned off using acetone and is ready for assembling the device components, as shown in figure 12.

B. Device Assembly

Figure 13 shows the schematics of the micro-receiver assembly process steps. First, two spacers are bonded to both

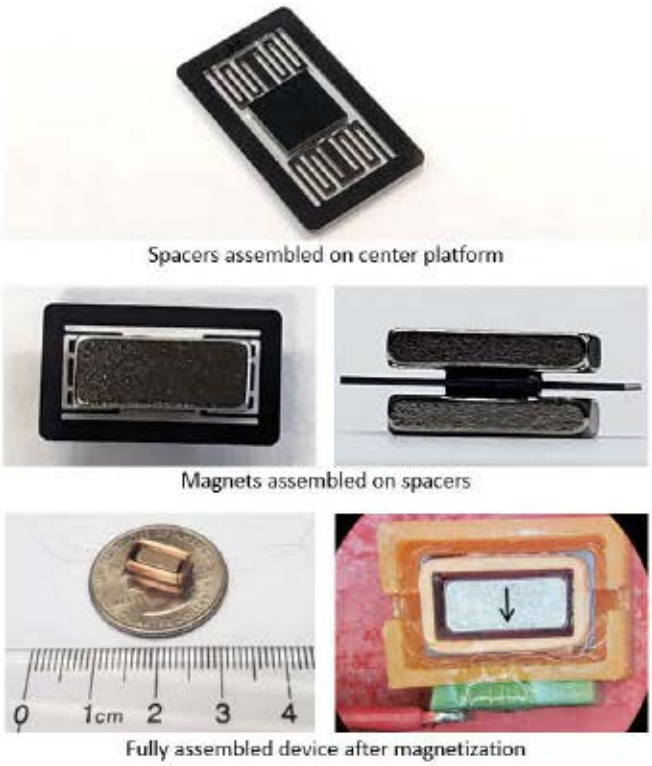

Fig. 14. Photographs of the assembled components and a fully assembled EWPT receiver prototype.

sides of the center platform of the serpentine suspension structure using cyanoacrylate. Two custom-manufactured (China Rare Earth Magnets Limited, Shenzhen, China), unmagnetized N52 NdFeB magnets ($7.8 \times 3.2 \times 1.6$ mm^3) are then glued to each spacer in such a way that the magnetic pole directions are parallel to each other. The magnets are delivered in an unmagnetized state because it is very difficult to accurately position the magnetized magnets if they magnetically repel each other. When the magnets are positioned, glued and cured, they are magnetized along the width by a pulse magnetizer (Model 340B, Oersted Technology). Two precision-manufactured (Precision Econowind LLC, Florida, USA) rectangular coils ($8.8 \times 4.2 \times 2.2$ mm^3) are then glued to both sides of the base frame. Each professionally wound coil is made of 44 AWG laminated copper magnet wire having 498 turns and 125 Ω resistance. The lateral airgap between the magnet and coil on each side is 0.5 mm that leaves sufficient clearance for ±11° rotation of the central structure. The volume of the fully assembled device is 0.31 cm^3 ($10.8 \times 6.2 \times 4.7$ mm^3) which is then disposed into a 3D printed housing for experimental characterization. The coils are connected in series and terminated to a printed circuit board (PCB) glued to the 3D printed package. Figure 14 shows the photographs of the assembled components and a fully assembled prototype.

IV. Experimental Characterization

A. Experimental Setup

The fabricated and assembled EWPT micro-receiver prototype was characterized under alternating magnetic fields of various amplitudes and frequencies generated by a transmitter

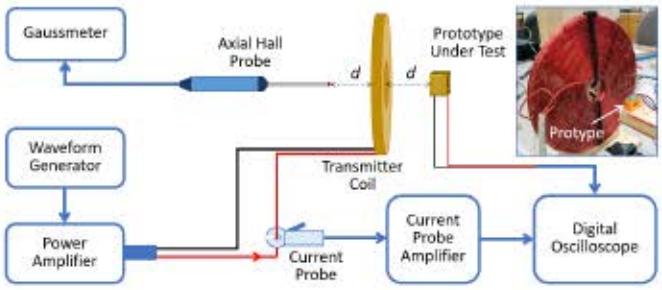

Fig. 15. Schematic block diagram and a photograph (inset) of the experimental characterization of the EWPT receiver prototype.

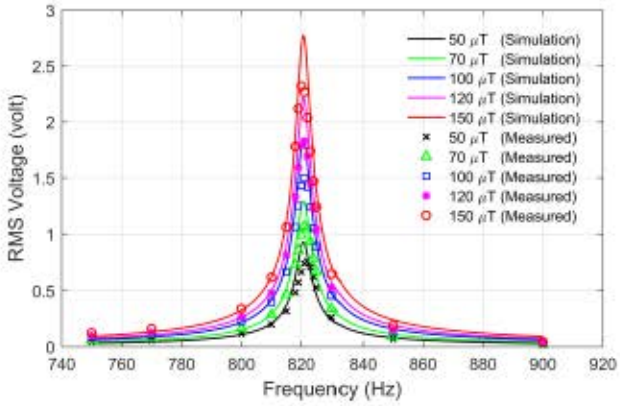

Fig. 16. Open-circuit voltage versus frequency of various magnetic fields at 4 cm on-axis distance from the transmitter coil.

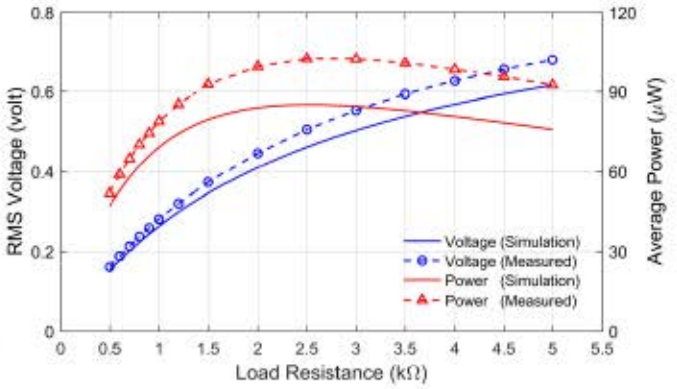

Fig. 17. Load voltage and time-average power versus load resistance for 50 μT_{rms} magnetic field at 821 Hz resonant frequency.

coil. Figure 15 shows the schematic block diagram and a photograph (inset) of the experimental setup. The 169-turn pancake-shaped transmitter coil (Ø15 cm × 1.5 cm) is made of 12 AWG laminated copper magnet wire, has a coil figure of merit $f_m = 13.4 \times 10^6$ W · T^{-2} [17] and generates uniaxial fields (i.e., at any given point, the field only increases and decreases in time, but does not change direction) around it. As seen from the block diagram, an arbitrary waveform generator (Rigol DG1022A) supplies AC voltage to a linear power amplifier (Crown K1) to generate an AC current which is fed to the transmitter coil. A current probe (Tektronix TCP312A) connected to a current probe amplifier (Tektronix TCPA300) monitors the AC current. A multi-channel digital storage oscilloscope (Tektronix DPO-2004 B) measures the input AC current to the transmitter coil as well as the output voltage generated by the EWPT micro-receiver prototype. An axial Hall probe (Lakeshore XHMMA-1482) connected to a gaussmeter (Lakeshore 475DSP) measures the resultant (for a given AC current) magnetic field generated by the transmitter coil. Note that, the Hall sensor (at the Hall probe tip) and the prototype under test are placed at opposite sides (on-axis and at the same distance, d) of the transmitter coil, assuming uniform B-field spatial distribution on both sides of the transmitter coil.

B. Results and Discussion

The frequency response of the fabricated EWPT micro-receiver is determined by measuring the open-circuit rms voltage as a function of frequency of the magnetic fields at various amplitudes (between 50 and 150 μT_{rms}). During this measurement, the prototype is fixed at 4 cm axial distance from the transmitter coil, and the current in the transmitter is adjusted to achieve the desired field at the location of the receiver. Figure 16 shows the simulated (solid lines) and measured (markers) response curves for various magnetic fields. As seen from the simulation, the micro-receiver exhibits a resonance around 821 Hz indicative of an underdamped 2nd-order system with high Q-factor (Q = 165 in air). However, the measurements exhibit slight nonlinear behavior, where the resonant frequency tends to shift lower as the amplitude of the applied magnetic field increases. Note that, the frequency of torsional resonance closely matches with the 3D-FEA model. A peak voltage sensitivity of the micro-receiver is measured as 15 V · mT^{-1} at 821 Hz resonant frequency.

Next, various load resistances are tested varying from 0.5 kΩ to 5 kΩ. Figure 17 shows both simulated (solid lines) and measured (dashed lines with markers) voltage and time-average power delivered to various load resistances while using a constant-amplitude, 50 μT_{rms} alternating magnetic field at 821 Hz resonance. The time-average power is calculated by using V_{rms}^2/R_L, where V_{rms} is the rms value of the measured voltage across each load resistance R_L. Results show that the rms voltage increases with the increase in the resistance value, however, a maximum power is obtained with an optimum load resistance of 2.5 kΩ. The value of optimum load resistance is 10× higher than the coil resistance (250 Ω), which indicates strong electrodynamic coupling in the receiver, implying strong electromechanical energy conversion. Referring to (11), the electrodynamic coupling strength is calculated as $\gamma = 9$.

Next, the magnetic field amplitude was varied, while keeping the frequency constant at 821 Hz and using the previously determined optimal load resistance of 2.5 kΩ. Figure 18 shows the simulated (solid lines) and measured (dashed lines with markers) voltage and time-average power for various magnetic fields. Simulation results show that the voltage increases linearly, whereas the time-average power increases quadratically with the increase in the magnetic field. The measurements also follow the same trend, however, for higher magnetic fields

TABLE III

PERFORMANCE COMPARISON AMONG VARIOUS STATE-OF-THE-ART EWPT SYSTEMS

Ref.	Transmitter Type	Receiver Type	Frequency (Hz)	Receiver Volume (cm^3)	B-field (mT)	Max. Power (mW)	Power Density ($mW \cdot cm^{-3}$)	NPD ($mW \cdot cm^{-3} \cdot mT^{-2}$)
[14]	Single pancake coil	ED	54	21.6	–	3.1	0.14	–
[15]	Helmholtz coil pair	ED	355	0.16	0.4	0.27	1.69	10.6
[16]	Rotating Magnet	ED	17	5.5	<1	22	4	–
[19]	Helmholtz coil pair	PE	95.6	1.2	0.1	0.014	0.012	1.2
[20]	Helmholtz coil pair	PE	260	4	0.13	0.005	0.0012	0.07
[21]	Single pancake coil	PE	211	2.5	0.83	3.3	1.3	1.89
[22]	Helmholtz coil pair	ED	744	0.55	0.55	2.5	4.6	15.2
This work	Single pancake coil	ED	821	0.31	0.6	2.46	7.9	21.9

ED = Electrodynamic, PE = Piezoelectric, NPD = Normalized Power Density.

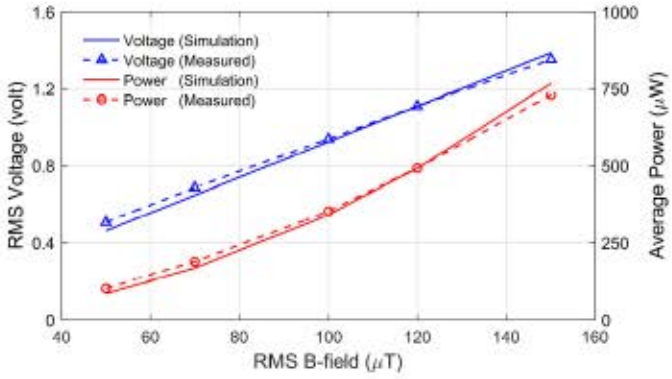

Fig. 18. Load voltage and time-average power delivered to 2.5 kΩ optimum load under various magnetic fields at 821 Hz resonant frequency.

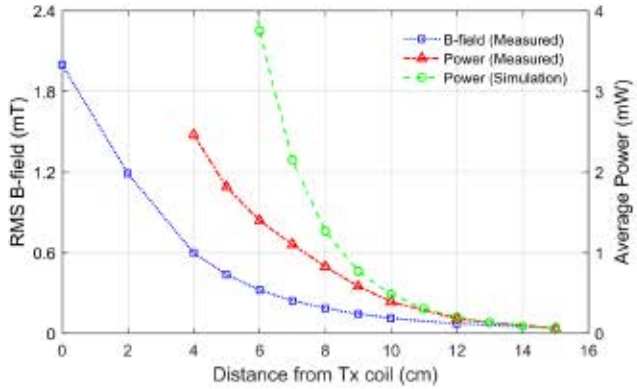

Fig. 19. Output power and magnetic field versus on-axis distance between the transmitter coil and micro-receiver while a maximum allowable safe field of 2 mT_{rms} at 821 Hz was generated at the center of the coil.

(over 120 μT_{rms}), the output power tends to increase slowly and reaches up to 730 μW for 150 μT_{rms} magnetic field, whereas the model predicts 766 μW. This discrepancy occurs due to the nonlinear behavior of the receiver observed earlier in the frequency response analysis (figure 16).

Finally, the time-average load power is measured as a function of distance (up to 15 cm) between the transmitter coil and the receiver, as shown in figure 19. In this case, a maximum of 2 mT_{rms} field at 821 Hz frequency (kept within human exposure safety limit) was generated right on the surface at the center of the coil by limiting the current to 614 mA_{rms}. As shown in figure 19, the micro- receiver generated a maximum of 2.46 mW average power at a distance of 4 cm from the coil, which corresponds to 7.9 $mW \cdot cm^{-3}$ power density. It is obvious that the magnetic field weakens as the distance from the transmitter coil increases, so too does the power generated by the receiver. However, the device is still able to generate meaningful power (61 μW) at a distance of 15 cm where the magnetic field strength was measured as low as 41 μT_{rms}.

Here, the measured power values are much lower than the simulated power values as the receiver is moved closer the transmitter coil. While the receiver operates at stronger field amplitudes, any system nonlinearities will become more evident. One aspect is a potential mechanical spring stiffening effect. Therefore, the resonant frequency moves further away from the 821 Hz resonance (at which all the measurements were taken). Additionally, the receiver electrodynamic coupling coefficient K_R is kept constant ($K_R = 0.011\ V \cdot s \cdot rad^{-1}$) in the simulation. However, in practice, K_R changes with the change in the magnetic field amplitude, since the angular displacements increase (see figure 9). These nonlinear analyses are beyond the scope of this manuscript and will be further analyzed in a future work.

V. CONCLUSION

In this work, we have presented the design, modeling, fabrication and characterization of an EWPT micro-receiver using a precision manufactured electrodynamic transducer on a bulk-micromachined Si serpentine torsional suspension for low-frequency electrodynamic WPT, aiming at wearable and implantable medical devices applications. The serpentine structure was designed by analyzing various torsional suspension structures with the help of finite-element analysis (FEA). A compact and volume-efficient electrodynamic transducer was designed, fabricated, assembled and tested within the safe exposure limit of electromagnetic fields, 2 mT_{rms}. Compared to a previous design [22], this new architecture offers significantly increased electrodynamic coupling strength (9 vs. 0.47) and larger voltage sensitivity (15 $V \cdot mT^{-1}$ vs. 0.95 $V \cdot mT^{-1}$). Furthermore, as shown in Table III, this device also yields the highest power density (7.9 $mW \cdot cm^{-3}$) and highest reported normalized power density (21.9 $mW \cdot cm^{-3} \cdot mT^{-2}$) when compared to all other reported EWPT devices. An equivalent

lumped-element circuit model has been established to predict the output performance of the proposed EWPT system. Experimental results are in good agreement with the simulation results, however, there are deviations at higher field amplitudes (over 150 μT_{rms}) due to un-modeled nonlinearities.

APPENDIX

From the simplified equivalent circuit model (Fig. 10), the load voltage across a resistive load R_L is

$$V_L = \frac{R_L}{R_R + R_L} V_{ind} \tag{A1}$$

According to gyrator principle [25], the voltage induced in the coil V_{ind} is given by

$$V_{ind} = K_R \dot{\theta} = K_R \frac{\tau_{mag}}{Z_m} \tag{A2}$$

where Z_m is the mechanical impedance of the receiver, expressed as

$$Z_m = \left(b + j\omega J + \frac{k}{j\omega}\right) + \frac{K_R^2}{R_R + R_L} \tag{A3}$$

Substituting (A3) and (A2) into (A1) yields

$$V_L = \frac{\tau_{mag} K_R}{\left(b + j\omega J + \frac{k}{j\omega}\right)(R_R + R_L) + K_R^2} R_L \tag{A4}$$

The total electrical output impedance Z_{out} at the receiver terminals is

$$Z_{out} = \frac{K_R^2}{b + j\omega J + \frac{k}{j\omega}} + R_R \tag{A5}$$

REFERENCES

[1] M. Song, P. Belov, and P. Kapitanova, "Wireless power transfer inspired by the modern trends in electromagnetics," *Appl. Phys. Rev.*, vol. 4, no. 2, Jun. 2017, Art. no. 021102.

[2] R. Shukla, N. Kiran, R. Wang, J. Gummeson, and S. I. Lee, "SkinnyPower: Enabling batteryless wearable sensors via intra-body power transfer," in *Proc. 17th Conf. Embedded Netw. Sensor Syst.*, New York, NY, USA, Nov. 2019, pp. 68–82.

[3] K. Agarwal, R. Jegadeesan, Y.-X. Guo, and N. V. Thakor, "Wireless power transfer strategies for implantable bioelectronics," *IEEE Rev. Biomed. Eng.*, vol. 10, pp. 136–161, Mar. 2017.

[4] A. Garraud and D. P. Arnold, "Advancements in electrodynamic wireless power transmission," in *Proc. IEEE Sensors*, Orlando, FL, USA, Oct. 2016, pp. 82–84.

[5] A. M. Jawad, R. Nordin, S. K. Gharghan, H. M. Jawad, and M. Ismail, "Opportunities and challenges for near-field wireless power transfer: A review," *Energies*, vol. 10, no. 7, p. 1022, Jul. 2017.

[6] D. Kim, A. Abu-Siada, and A. Sutinjo, "State-of-the-art literature review of WPT: Current limitations and solutions on IPT," *Electr. Power Syst. Res.*, vol. 154, pp. 493–502, Jan. 2018.

[7] S. D. Barman, A. W. Reza, N. Kumar, M. E. Karim, and A. B. Munir, "Wireless powering by magnetic resonant coupling: Recent trends in wireless power transfer system and its applications," *Renew. Sustain. Energy Rev.*, vol. 51, pp. 1525–1552, Nov. 2015.

[8] *Standard for Safety Levels With Respect to Human Exposure to Radio Frequency Electromagnetic Fields, 3 kHz to 300 GHz*, IEEE Standard C95.1-2010, Mar.2010, pp. 1–238.

[9] *Standard for Safety Levels With Respect to Human Exposure to Electromagnetic Fields, 0-3 kHz*, IEEE Standard C95.6-2002, Oct. 2002, pp. 1–43.

[10] D.-X. Yang, Z. Hu, H. Zhao, H.-F. Hu, Y.-Z. Sun, and B.-J. Hou, "Through-metal-wall power delivery and data transmission for enclosed sensors: A review," *Sensors*, vol. 15, no. 12, pp. 31581–31605, Dec. 2015.

[11] W. Li, "High efficiency wireless power transmission at low frequency using permanent magnet coupling," M.S. Thesis, Dept. Phys. Astron., Univ. British Columbia, Vancouver, BC, Canada, Aug. 2009.

[12] V. R. Challa, J. O. Mur-Miranda, and D. P. Arnold, "Wireless power transmission to an electromechanical receiver using low-frequency magnetic fields," *Smart Mater. Struct.*, vol. 21, no. 11, Oct. 2012, Art. no. 115017.

[13] H. Jiang *et al.*, "A low-frequency versatile wireless power transfer technology for biomedical implants," *IEEE Trans. Biomed. Circuits Syst.*, vol. 7, no. 4, pp. 526–535, Aug. 2013.

[14] K. M. McEachern and D. P. Arnold, "Electrodynamic wireless power transmission to a torsional receiver," *J. Phys., Conf. Ser.*, vol. 476, Dec. 2013, Art. no. 012004.

[15] S. Du, E. K. Chan, B. Wen, J. Hong, H. Widmer, and C. E. Wheatley, "Wireless power transfer using oscillating magnets," *IEEE Trans. Ind. Electron.*, vol. 65, no. 8, pp. 6259–6269, Aug. 2018.

[16] N. Garraud, D. Alabi, S. Chyczewski, J. D. Varela, D. P. Arnold, and A. Garraud, "Extending the range of wireless power transmission for bio-implants and wearables," *J. Phys., Conf. Ser.*, vol. 1052, Jul. 2018, Art. no. 012023.

[17] N. Garraud, A. Garraud, D. Munzer, M. Althar, and D. P. Arnold, "Modeling and experimental analysis of rotating magnet receivers for electrodynamic wireless power transmission," *J. Phys. D, Appl. Phys.*, vol. 52, no. 18, Feb. 2019, Art. no. 185501.

[18] I. Paprotny *et al.*, "Piezoelectrodynamic gyrator: Analysis experiments and applications to wireless power transfer," in *Proc. PowerMEMS*, Atlanta, GA, USA, Dec. 2012, pp. 166–263.

[19] G. Liu, P. Ci, and S. Dong, "Energy harvesting from ambient low-frequency magnetic field using magneto-mechano-electric composite cantilever," *Appl. Phys. Lett.*, vol. 104, no. 3, Jan. 2014, Art. no. 032908.

[20] B. D. Truong and S. Roundy, "Wireless power transfer system with center-clamped magneto-mechano-electric (MME) receiver: Model validation and efficiency investigation," *Smart Mater. Struct.*, vol. 28, no. 1, Jan. 2019, Art. no. 015004.

[21] M. A. Halim, J. M. Samman, S. E. Smith, and D. P. Arnold, "Piezoceramic electrodynamic wireless power receiver using torsion mode meandering suspension," in *Proc. PowerMEMS*, Krakow, Poland, Dec. 2019, Art. no. 20515809768.

[22] N. Garraud, D. Alabi, J. D. Varela, D. P. Arnold, and A. Garraud, "Microfabricated electrodynamic wireless power receiver for bio-implants and wearables," in *Solid-State, Actuat., Microsyst. Workshop Tech. Dig.*, Hilton Head Island, SC, USA, May 2018, pp. 34–37.

[23] M. A. Halim, S. E. Smith, J. M. Samman, and D. P. Arnold, "A high-performance electrodynamic micro-receiver for low-frequency wireless power transfer," in *Proc. IEEE 33rd Int. Conf. Micro Electro Mech. Syst. (MEMS)*, Vancouver, BC, Canada, Jan. 2020, pp. 590–593.

[24] S. Cheng, N. Wang, and D. P. Arnold, "Modeling of magnetic vibrational energy harvesters using equivalent circuit representations," *J. Micromech. Microeng.*, vol. 17, no. 11, pp. 2328–2335, Oct. 2007.

[25] S. D. Senturia, *Microsystem Design*. New York, NY, USA: Springer, 2001. [Online]. Available: https://www.springer.com/gp/book/9780792372462

[26] V. R. Challa, S. Cheng, and D. P. Arnold, "The role of coupling strength in the performance of electrodynamic vibrational energy harvesters," *Smart Mater. Struct.*, vol. 22, no. 2, Feb. 2013, Art. no. 025005.

[27] H. Allag and J.-P. Yonnet, "3-D analytical calculation of the torque and force exerted between two cuboidal magnets," *IEEE Trans. Magn.*, vol. 45, no. 10, pp. 3969–3972, Oct. 2009.

Miah A. Halim received the B.S. and M.S. degrees in applied physics electronics and communication engineering from Islamic University, Kushtia, Bangladesh, in 2008 and 2010, respectively, and the Ph.D. degree in electronic engineering from Kwangwoon University, Seoul, South Korea, in 2016, in energy harvesting from low-frequency and human-body-induced motions.

Later, he worked on energy harvesting for wearable smart devices applications at the Mechanical Engineering Department, The University of Utah, Salt Lake City. He is currently a Post-Doctoral Research Associate and a member of the Interdisciplinary Microsystems Group (IMG), Electrical and Computer Engineering Department, University of Florida, Gainesville. His current research focuses on magnetic microsystems for low-power applications. His main research interests include electromechanical transducers, multi-source energy harvesting, electrodynamic wireless power transmission systems, and multifunctional materials and systems.

Adrian A. Rendon-Hernandez received the B.S. degree in electronics and communication engineering from the Autonomous University of Nuevo Leon, San Nicolas de los Garza, Mexico, in 2008, the M.S. degree in electronics systems engineering from the Monterrey Institute of Technology, Monterrey, Mexico, in 2012, and the Ph.D. degree in nanoelectronics and nanotechnologies from Grenoble Alpes University, Grenoble, France, in 2018.

He worked on advanced simulations for industrial sensors and actuators at Schneider Electric, Mexico, as an Research and Development Engineer. He is currently a Post-Doctoral Research Associate and a member of the Interdisciplinary Microsystems Group (IMG), Electrical and Computer Engineering Department, University of Florida, Gainesville. His research interests include the area of design, modeling, and characterization of wireless power transmission and energy harvesting devices.

Spencer E. Smith received the B.S. degree in aerospace engineering and mechanical engineering from the University of Florida, Gainesville, FL, USA, in 2020. Since 2019, he has been working as an Undergraduate Research Student with the Interdisciplinary Microsystems Group, University of Florida. His research interests include electrodynamic wireless power transmission system with a focus on the design, fabrication, and testing of wireless power receivers.

Joseph M. Samman received the B.S. degree in electrical engineering from the University of Florida, Gainesville, in 2020, where he is currently pursuing the M.S. degree in electrical engineering. Since September of 2018, he has been working as an Undergraduate Researcher with the Interdisciplinary Microsystems Group (IMG), University of Florida, under his faculty mentor Dr. D. P. Arnold. His research interests include wireless power MEMS and analog IC design.

Nicolas Garraud received the B.S. degree in mechanical engineering from ENS Cachan in 2002, the M.S. degree in mechanical engineering from University Paris 6, France, in 2005, and the Ph.D. degree in electrical engineering from the University of Florida, Gainesville, USA, in 2018.

He is currently a Research Engineer with CEA-LETI, a research institute for electronics and information technologies at the French Alternative Energies and Atomic Energy Commission, Grenoble, France. He was a recipient of a two-year-long European individual fellowship from Marie Skłodowska-Curie Actions in 2019. His research interests include wireless power transmission and energy harvesting solutions for industrial and biomedical applications.

David P. Arnold (Senior Member, IEEE) received the dual B.S. degree in electrical and computer engineering and the M.S. degree in electrical and computer engineering from the University of Florida, Gainesville, in 1999 and 2001, respectively, and the Ph.D. degree in electrical and computer engineering from the Georgia Institute of Technology, Atlanta, in 2004.

He is currently the George Kirkland Engineering Leadership Professor and Associate Chair for Research with the Department of Electrical and Computer Engineering, University of Florida, the Deputy Director of the NSF Multi-Functional Integrated System Technology (MIST) Center, and a member of the UF Interdisciplinary Microsystems Group (IMG). He has coauthored over 200 refereed journal and conference publications and holds 22 U.S. patents. His research interests include micro/nanostructured magnetic materials, magnetic microsystems, electromechanical transducers, and miniaturized power/energy systems.

Dr. Arnold is a member of Tau Beta Pi and Eta Kappa Nu. His research innovations have been recognized by the 2008 Presidential Early Career Award in Science and Engineering (PECASE) and the 2009 DARPA Young Faculty Award. He is an active participant in the magnetics and MEMS communities, with ongoing involvement in various conference committees, and currently serving on the editorial boards of Micromachines and J. Micromechanics and Microengineering.